

Particle Patterning by Ultrasonic Standing Waves in a Rectangular Cavity


Glauber T. Silva,^{1,*} José H. Lopes,² José P. Leão-Neto,³ Madeleine K. Nichols,⁴ and Bruce W. Drinkwater⁴

¹*Physical Acoustics Group, Instituto de Física, Universidade Federal de Alagoas, Maceió, Alagoas 57072-970, Brazil*

²*Grupo de Física da Matéria Condensada, Núcleo de Ciências Exatas, Universidade Federal de Alagoas, Arapiraca, Alagoas 57309-005, Brazil*

³*Campus Arapiraca/Unidade de Ensino Penedo, Universidade Federal de Alagoas, Penedo, Alagoas 57200-000, Brazil*

⁴*Department of Mechanical Engineering, University of Bristol, Bristol BS8 1TR, United Kingdom*

 (Received 27 February 2019; revised manuscript received 11 April 2019; published 16 May 2019)

Different types of particle and/or cell patterning in acoustic cavities produced by the radiation force of ultrasonic standing waves have been observed. However, most explanations of this phenomenon are constrained to particles much smaller than the wavelength (i.e., the so-called Rayleigh regime). Here, we present a theoretical model for acoustic trapping and patterning of particles/cells in a rectangular cavity beyond the Rayleigh regime. A simple closed-form expression of the radiation-force potential for particles of virtually any size immersed in a fluid is obtained. Particles with a size comparable to one wavelength (Mie particles) can be trapped in acoustic potential wells, whose stability is quantified by the trap stiffness. Our findings reveal that an acoustic trap can occur at a pressure node, antinode, and midpoint (i.e., a point midway between two nodes). These locations depend on the acoustic parameters of the particle and surrounding fluid (density, longitudinal, and shear speed of sound) and the ratio of particle size to wavelength. We also investigate the effects of the secondary radiation forces on trapping stability. We determine the possible acoustic patterns formed with polystyrene particles and osmotically swollen red blood cells (SRBCs). The conditions that may lead to one particle/cell per acoustic well patterning are discussed. A set of patterning experiments is performed with an acoustofluidic rectangular device, operating at 6.5-MHz frequency, using polystyrene particles with diameters of 10 μm (Rayleigh particles) and 75 μm (Mie particles) immersed in distilled water. The obtained experimental results are consistent with our theoretical predictions. The present study can help in designing acoustofluidic devices with the ability to spatially arrange larger, or more closely spaced particles, cells, and other micro-organisms.

DOI: [10.1103/PhysRevApplied.11.054044](https://doi.org/10.1103/PhysRevApplied.11.054044)

I. INTRODUCTION

The ability to trap particles such as cells, micro-organisms, and biochemical compounds with the acoustic radiation force of ultrasonic waves is fostering a revolution in biotechnology and analytical chemistry [1,2]. In recent years, there has been a growing interest in developing acoustic devices for trapping and patterning individual cells, particles, and chemical compounds [3–13]. Cell patterning in microwell arrays is becoming a useful tool in single-cell analysis [14], which includes applications in intracellular research, gene and protein content and expression, polymerase chain reaction, cell culture and division, clone formation, differentiation, morphology, lysis, separation, sorting, cytotoxicity and fluorescence screens, and antibody secretion.

Two lab-on-a-chip technologies are employed to acoustically pattern particles, droplets, and cells, namely surface (SAW) [3,5,8,11] and bulk (BAW) [6,7,9] acoustic wave devices. In a common arrangement, SAW patterning devices have a three-dimensional (3D) rectangular-prism chamber bounded in the manipulation plane by four piezoelectric interdigital transducers (IDTs) operating at the same frequency that generates a two-dimensional (2D) surface standing wave. The surface waves leak into the device's chamber, yielding two orthogonal standing waves. Likewise, BAW devices consist of four piezoelectric transducers forming a chamber in which two orthogonal standing waves are generated. The acoustic waves are produced directly into the liquid within the chamber. Both SAW and BAW technologies generate acoustic traps that correspond to the radiation-force potential minima, referred to as acoustic potential wells.

*gtomaz@fis.ufal.br

Acoustic energy landscapes generated in a rectangular cavity have been theoretically studied for the case of a particle with a diameter much smaller than the wavelength (Rayleigh particles) [15]. The analysis is based on Gor'kov potential theory [16,17]. In fact, most investigations of acoustofluidic devices for 2D patterning ultimately rely on this theory [3,7,8,11,18,19], which cannot be used to describe the radiation force on particles whose diameters are comparable with the wavelength (Mie particles) or above.

A previous theoretical study of the acoustic radiation force exerted on Mie particles by a one-dimensional (1D) standing wave revealed that the force depends on the acoustic properties of the particle, with resonances that are functions of the frequency-radius product [20]. As an alternative, one can use the finite-element (FE) method to compute the radiation force of the problem [21].

Based on FE simulations, a detailed study of the one cell per acoustic potential well (OCPW) patterning of polymer particles and cells in a 1D standing wave has been performed [22]. The authors of this study unveiled the presence of resonances in the primary radiation force and analyzed the influence of the secondary radiation force in different particle spatial configurations. In another investigation, a many-particle dynamics simulation was carried out using a 3D-FE model to compute the acoustic energy landscapes including the secondary radiation force [23]. Nevertheless, numerical FE models do not necessarily provide a clear understanding of patterning as they are essentially only virtual experiments. Computing a particle trajectory in a 16-particle dynamics simulation is time consuming, taking at least 6 h [23]. The computational simulation time could be dramatically reduced if a closed-form solution of the acoustic landscapes were available. Simulations of this kind are a crucial step to engineer acoustofluidic patterning devices.

The lack of a comprehensive theoretical investigation of acoustic energy landscapes beyond Rayleigh particles has prompted us to develop the analytical model presented here. In addition, our theoretical findings may provide insights on the OCPW patterning technique for massively parallel single-cell analysis. This method has been demonstrated experimentally for Mie particles only [8,13].

The paper is organized as follows. Section II presents the scattering and acoustic radiation-force theories based on the partial-wave expansion method. A closed-form expression of the acoustic energy landscape of a 2D standing wave is obtained. The stability of acoustic traps and the effects of secondary radiation forces are also analyzed in this section. In Sec. III, we analyze the acoustic patterning of polystyrene particles and osmotically swollen red blood cells (SRBCs). Experimental results for patterning Rayleigh and Mie polystyrene particles are presented in Sec. IV. Finally, our key findings are summarized in Sec. V.

II. PHYSICAL MODEL

Consider a liquid of infinite extent characterized by sound speed c_0 and density ρ_0 . A spherical particle of radius a is placed in the fluid at an arbitrary position $\mathbf{r}_1 = x_1 \mathbf{e}_x + z_1 \mathbf{e}_z$, where \mathbf{e}_x and \mathbf{e}_z are the Cartesian unit vectors. The particle is made of a solid elastic material with density ρ_1 and longitudinal and shear speed of sound denoted by c_L and c_S , respectively. Thermoviscous effects on the particle can be induced within the viscous and thermal boundary layers by an ultrasonic wave of angular frequency ω . The boundary layer thicknesses scale approximately as $\omega^{-1/2}$ [24]. We shall present experimental results for an acoustic patterning device operating at 6.5 MHz in water at room temperature. In this case, the viscous and thermal boundary layer thicknesses are 0.20 and 0.085 μm , respectively. Hence, these boundary layers are much smaller than the polystyrene particles that will be considered here (with diameters of 10 and 75 μm). Therefore, we assume that the surrounding liquid is a lossless fluid. In addition, the streaming-induced drag forces on particles with diameter above 2 μm are much smaller than the acoustic radiation force [25], and so acoustic streaming is also neglected in our analysis.

A. 2D standing wave

In both SAW and BAW devices, the acoustic waves are generated in a 3D chamber with a rectangular base. Usually, the chamber's height is much smaller than the other orthogonal dimensions [7,8,10,26]. We thus assume that the device can be approximated in two dimensions as a rectangular cavity and the acoustic field can be represented by the superposition of two orthogonal standing waves of angular frequency ω . The incident pressure amplitude to the particle inside the chamber is given by

$$p_{\text{in}}(\mathbf{r}|\mathbf{r}_1) = \frac{p_0}{2} \{ \epsilon \cos[k(x + x_1)] + \cos[k(z + z_1)] \}, \quad (1)$$

where p_0 is the pressure magnitude, ϵ is the dimensionless amplitude of the standing wave along the x axis, $k = 2\pi/\lambda$ is the wave number, and $r_1 = \sqrt{x_1^2 + z_1^2}$ is the distance from the particle to the antinode at $x = 0$ and $z = 0$. The time-harmonic term in Eq. (1) is suppressed for simplicity.

For SAW devices, the refracted wave into the chamber moves along the direction given by a refraction angle known as the Rayleigh angle [5] $\theta_R = \arcsin(c_0/c_{\text{SAW}})$, where c_{SAW} denoted the sound speed of the piezoelectric substrate. The wavelength in SAW devices is expressed by $\lambda = 2\pi(c_0/\omega) \sin^{-1} \theta_R$. For the case of a BAW device, the Rayleigh angle is set to $\theta_R = 90^\circ$ and $\lambda = 2\pi c_0/\omega$.

In Fig. 1, we depict the pressure amplitude of the 2D standing wave normalized to p_0 , with $\epsilon = 1$. The pressure

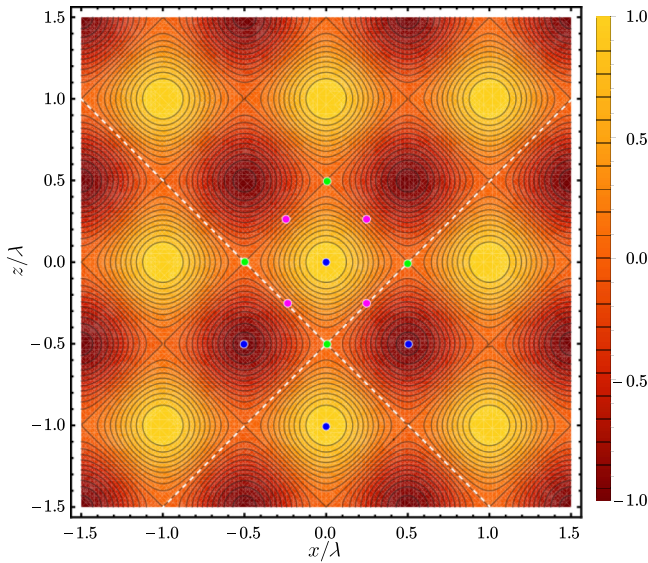


FIG. 1. Normalized pressure amplitude of the 2D standing wave given by Eq. (1) with $\epsilon = 1$ and $x_1 = z_1 = 0$. The pressure nodes (green dots), antinodes (blue dots), midpoints (purple dots), and nodal lines (white dashed lines) are illustrated.

antinodes and nodes are located, respectively, as

$$\mathbf{r}_{nm}^{(A)} = \left\{ \begin{array}{l} (n, m) \lambda, \\ \left(\frac{2n+1}{2}, \frac{2m+1}{2} \right) \lambda, \end{array} \right. \quad \mathbf{r}_{nm}^{(N)} = \left\{ \begin{array}{l} \left(n, \frac{2m+1}{2} \right) \lambda, \\ \left(\frac{2n+1}{2}, m \right) \lambda, \end{array} \right. \quad (2)$$

with $n, m \in \mathbb{Z}$. The lines linking two nearest nodes are referred to as nodal lines. A midpoint is a point equidistant to two nodes in a nodal line, whose position is

$$\mathbf{r}_{nm}^{(M)} = \left(\pm \frac{2n+1}{4}, \pm \frac{2m+1}{4} \right) \lambda. \quad (3)$$

B. Acoustic scattering

To determine the acoustic radiation force on a particle, we have to solve the corresponding scattering problem for a solid elastic particle in an ideal fluid. The coordinate system origin is set at the particle's center. It is useful to express the incident pressure given in Eq. (1) in terms of the partial-wave series in spherical coordinates (r, θ, φ) ,

$$p_{\text{in}} = p_0 \sum_{n,m} a_{nm}(x_1, z_1) j_n(kr) Y_n^m(\theta, \varphi), \quad (4)$$

where $\sum_{n,m} = \sum_{n=0}^{\infty} \sum_{m=-n}^n$ and j_n is the n th-order spherical Bessel function. The spherical harmonic of n th order

and m th degree is

$$Y_n^m(\theta, \varphi) = \sqrt{\frac{2n+1}{4\pi} \frac{(n-m)!}{(n+m)!}} P_n^m(\cos \theta) e^{im\varphi}, \quad (5)$$

with P_n^m being the associated Legendre polynomial [27]. In Appendix A, we derive the expansion coefficient a_{nm} also known as the beam-shape coefficient. Referring to Eq. (A3) we find

$$a_{nm}(x_1, z_1) = \sqrt{4\pi(2n+1) \frac{(n-m)!}{(n+m)!}} \times \left[\delta_{m,0} \cos\left(kz_1 + \frac{n\pi}{2}\right) + \epsilon P_n^m(0) \cos\left(kx_1 + \frac{n\pi}{2}\right) \right], \quad (6)$$

where δ_{nm} is the Kronecker's delta function. Here, we use $P_n^m(1) = \delta_{m,0}$.

The pressure amplitude of the scattered wave is also given by a partial-wave series,

$$p_{\text{sc}} = p_0 \sum_{n,m} a_{nm}(x_1, z_1) s_n h_n^{(1)}(kr) Y_n^m(\theta, \varphi), \quad (7)$$

where $h_n^{(1)}$ is the n th-order spherical Hankel function of the first type and s_n is the scattering coefficient. This coefficient is obtained by applying the continuity condition of the acoustic fields (radial and tangential stresses and fluid velocity) across the particle's surface. Accordingly, the scattering coefficients of a solid elastic particle are given by [28]

$$s_n = \det \begin{bmatrix} e_1 & d_{12} & d_{13} \\ e_2 & d_{22} & d_{23} \\ 0 & d_{32} & d_{33} \end{bmatrix} \det \begin{bmatrix} d_{11} & d_{12} & d_{13} \\ d_{21} & d_{22} & d_{23} \\ 0 & d_{32} & d_{33} \end{bmatrix}^{-1}. \quad (8)$$

The matrix elements e_1, e_2, d_{ij} (with $i, j = 1, 2, 3$) are given in Appendix C.

C. Primary acoustic radiation force

The primary radiation force caused by an acoustic wave on a particle is given by [29]

$$\mathbf{F}_{\text{rad}} = \pi a^2 E_0 \mathbf{Q}_{\text{rad}}, \quad (9)$$

where $E_0 = p_0^2 / 2\rho_0 c_0^2$ is the characteristic energy of the wave and

$$\mathbf{Q}_{\text{rad}} = (Q_x \mathbf{e}_x + Q_z \mathbf{e}_z) \quad (10)$$

is the radiation-force efficiency. The Cartesian components of the radiation-force efficiency vector \mathbf{Q}_{rad} are given

by [30,31]

$$Q_x = -\frac{1}{2\pi(ka)^2} \text{Im} \sum_{n,m} \sqrt{\frac{(n+m+1)(n+m+2)}{(2n+1)(2n+3)}} \\ \times (S_n a_{nm} a_{n+1,m+1}^* + S_n^* a_{n,-m}^* a_{n+1,-m-1}), \quad (11a)$$

$$Q_z = \frac{1}{\pi(ka)^2} \text{Im} \sum_{n,m} \sqrt{\frac{(n-m+1)(n+m+1)}{(2n+1)(2n+3)}} \\ \times S_n a_{nm} a_{n+1,m}^*, \quad (11b)$$

where an asterisk denotes complex conjugation and $S_n = s_n + s_{n+1}^* + 2s_n s_{n+1}^*$.

After substituting the beam-shape coefficients given in Eq. (6) into Eq. (11), we obtain the radiation-force efficiencies as

$$Q_x = \epsilon Q_1 \sin kx \cos kz + \epsilon^2 Q_2 \sin 2kx, \quad (12a)$$

$$Q_z = \epsilon Q_1 \sin kz \cos kx + Q_2 \sin 2kz. \quad (12b)$$

For the sake of simplicity, we drop the indexes of x_1 and z_1 in these equations. The auxiliary radiation-force efficiencies are expressed by

$$\begin{bmatrix} Q_1 \\ Q_2 \end{bmatrix} = -\frac{2}{(ka)^2} \sum_{n=0}^{\infty} \begin{bmatrix} \varepsilon_n - \varepsilon_{n+1} \\ (-1)^n \end{bmatrix} (n+1) \text{Im}[S_n], \quad (13)$$

where $\varepsilon_n = [1 + (-1)^n] P_n(0)$. The functions Q_1 and Q_2 correspond, respectively, to how efficiently the crossed and 1D radiation-force components given in Eq. (12) develop on the particle. They depend on the acoustic properties of the particle and surrounding liquid. Note that, as expected, the expression obtained for Q_2 agrees with the result for the 1D radiation force of a standing wave field [see Eq. (27) in Ref. [20]].

D. Acoustic energy landscape

Similarly to Gor'kov's theory of the acoustic radiation force on Rayleigh particles [16], we introduce the radiation-force potential U by direct integration of Eq. (12) over x and z . Accordingly,

$$\mathbf{F}_{\text{rad}} = -\nabla U, \quad (14)$$

where

$$U(x, z) = \frac{3V_1 E_0}{8ka} (\epsilon^2 Q_2 \cos 2kx + 2\epsilon Q_1 \cos kx \cos kz \\ + Q_2 \cos 2kz) + U_0, \quad (15)$$

with $V_1 = 4\pi a^3/3$ being the particle volume and U_0 being an arbitrary integration constant. Equation (15) is valid for

large particles whose size is comparable to the wavelength, i.e., Mie particles. This result generalizes the acoustic energy landscape obtained in Ref. [26] that is valid only for Rayleigh particles.

E. Acoustic trap stability

In a trapping point \mathbf{r}_{trap} , the acoustic radiation force is zero (potential well). Acoustic traps may take place at pressure nodes and/or antinodes described in Eq. (2) and in the midpoints given by Eq. (3). After expanding the efficiencies in Eq. (12) around $\mathbf{r} = \mathbf{r}_{\text{trap}}$, we find

$$\mathbf{F}_{\text{rad}} = -\mathbf{K}(\mathbf{r} - \mathbf{r}_{\text{trap}}), \quad (16)$$

where \mathbf{K} is the stiffness matrix, which is given for a node, antinode, and midpoint by

$$\mathbf{K}^{(N)} = \pi a^2 E_0 k \text{diag} (2\epsilon^2 Q_2 - \epsilon Q_1, 2Q_2 - \epsilon Q_1), \quad (17a)$$

$$\mathbf{K}^{(A)} = -\pi a^2 E_0 k \text{diag} (\epsilon Q_1 + 2\epsilon^2 Q_2, \epsilon Q_1 + 2Q_2), \quad (17b)$$

$$\mathbf{K}^{(M)} = -\pi a^2 E_0 k \begin{pmatrix} 2\epsilon^2 Q_2 & \epsilon Q_1 \\ \epsilon Q_1 & 2Q_2 \end{pmatrix}. \quad (17c)$$

The stiffness matrix should be positive definite to ensure trap stability; e.g., all matrix eigenvalues are positive. When the orthogonal standing waves have the same amplitude $\epsilon = 1$, we note that the traps are stable if

$$Q_1 - 2Q_2 > 0 \quad (\text{node}), \quad (18a)$$

$$Q_1 + 2Q_2 < 0 \quad (\text{antinode}), \quad (18b)$$

$$Q_1 - 2Q_2 < 0, \quad Q_1 + 2Q_2 > 0 \quad (\text{midpoint}). \quad (18c)$$

In this case, traps at pressure nodes and antinodes are circularly symmetric because the stiffness matrix has a degenerated eigenvalue, whereas those in midpoints have an elliptical shape since the corresponding eigenvalues are distinct.

Courtney *et al.* [7] have shown that the diagonal term $\cos kx \cos kz$ of Eq. (15) can be eliminated by adjusting the standing wave phases. This method was demonstrated for Rayleigh particles which, according to the conditions in Eq. (18), will be trapped in nodes and antinodes when $Q_2 < 0$ and in midpoints if $Q_2 > 0$. In both cases, the acoustic traps are circularly symmetric.

F. Secondary acoustic radiation force

When two or more particles are present in the medium, rescattering events give rise to the acoustic interaction forces between the particles. This force, also known as the secondary radiation force, can be either attractive or repulsive [32,33]. The secondary radiation forces can disturb the acoustic energy landscape of the primary radiation force.

Assume that a collection of N nonintersecting particles ($N \geq 2$) is suspended in a fluid. The position and radius of a particle are denoted, respectively, by \mathbf{r}_i and a_i ($i = 1, 2, \dots, N$). Consider that $\mathcal{P} = (\mathbf{r}_1, \dots, \mathbf{r}_{i-1}, \mathbf{r}_{i+1}, \dots, \mathbf{r}_N)$ represents the particle positions excluding \mathbf{r}_i . The incident effective pressure on the particle at \mathbf{r}_i is given by

$$p_{\text{eff}}^{(i)}(\mathbf{r}|\mathbf{r}_1, \dots, \mathbf{r}_N) = p_{\text{in}}(\mathbf{r}|\mathbf{r}_i) + p_{\text{sc}}(\mathbf{r}|\mathcal{P}), \quad (19)$$

where $p_{\text{sc}}(\mathbf{r}|\mathcal{P})$ is the total scattered pressure by particles at \mathcal{P} . In the reference frame set at \mathbf{r}_i , the pressure $p_{\text{sc}}(\mathbf{r}|\mathcal{P})$ is an analytic function. Hence, the effective pressure $p_{\text{eff},i}$ can be expanded into a partial-wave series as given in Eq. (4). Thus, we conclude that the beam-shape coefficient for the particle at \mathbf{r}_i is given by

$$c_{nm}^{(i)} = a_{nm}^{(i)} + b_{nm}^{(i)}, \quad (20)$$

where $a_{nm}^{(i)}$ is the beam-shape coefficient of the standing wave expressed by Eq. (6). The coefficient $b_{nm}^{(i)}$ is the expansion coefficient of the rescattered waves. It is determined with a seminumerical method based on the partial-wave expansion method and the addition theorem as presented in Appendix B.

After substituting Eq. (20) into Eq. (11) and following the same procedure to derive Eq. (14), we find the efficiency of the total radiation force exerted on the particle at \mathbf{r}_i as

$$\mathbf{Q}_{\text{tot}}^{(i)} = \mathbf{Q}_{\text{rad}}^{(i)} + \mathbf{Q}_{\text{int}}^{(i)}, \quad (21)$$

where $\mathbf{Q}_{\text{rad}}^{(i)}$ and $\mathbf{Q}_{\text{int}}^{(i)}$ are the efficiencies of the primary and secondary (interaction) radiation forces, respectively. The Cartesian components of the acoustic interaction force are given by the equations in Eq. (11) by setting $a_{nm} = b_{nm}^{(i)}$.

III. NUMERICAL RESULTS

We analyze now the acoustic radiation force exerted on polystyrene particles and osmotically SRBCs in water at room temperature. Polystyrene is chosen because it is routinely used as a calibration particle in acoustofluidic experiments as its acoustic properties are similar to cells. We assume that osmotically SRBCs can be modeled as a spherical fluid particle [34]. The physical parameters of polystyrene, SRBC, and surrounding liquid are

TABLE I. Physical parameters of a polystyrene particle and SRBC suspended in water at room temperature and pressure.

Description	Value
<i>Water</i>	
Density (ρ_0)	998 kg m ⁻³
Speed of sound (c_0)	1493 m s ⁻¹
<i>Polystyrene</i> [35]	
Density (ρ_1)	1052 kg m ⁻³
Longitudinal speed of sound (c_L)	2400 m s ⁻¹
Shear speed of sound (c_S)	1150 m s ⁻¹
<i>SRBC</i> [34]	
Density (ρ_1)	1139 kg m ⁻³
Longitudinal speed of sound (c_L)	1680 m s ⁻¹

given in Table I. In the upcoming analysis, it is useful to define the size parameter of the particle as the diameter-to-wavelength ratio,

$$\xi = \frac{2a}{\lambda}. \quad (22)$$

A. Radiation-force efficiencies

To compute the radiation-force efficiencies Q_1 and Q_2 , we have to establish a truncation order $n = M$ in Eq. (13). We adopt the Wiscombe's truncation criterion used in optics [36], which is based on the fact that for a fixed particle size parameter ξ , the contribution of an n th-scattering mode in Eq. (7) decreases as n increases. Accordingly, a truncation order of $M = 10$ suffices to compute the radiation force on particles with a wavelength diameter, $2a = \lambda$, or smaller.

In Fig. 2, we show the efficiencies Q_1 and Q_2 versus the size parameter ξ for (a) a polystyrene particle and (b) a SRBC. Equation (13) is used to evaluate the efficiencies numerically. The presence of resonances is noted in the radiation-force efficiencies of polystyrene. They can be understood in terms of the resonances that appear in the scattering modes described by the coefficients s_n [37]. The trapping band (N) node, (A) antinode, and (M) midpoint are determined and shown by using the conditions in Eq. (18). The bandwidths are summarized in Table II. Note that the Q_2 efficiency for a polystyrene particle shown in Fig. 2 is very similar to what has been obtained for a 1D standing wave with the FE method in Fig. 2(b) of Ref. [22].

B. Effects of the secondary radiation forces

To assess the effects of the secondary radiation forces on the trapping stability, we numerically compute these forces on two identical polystyrene particles, with size parameters $\xi < 0.47$. The 2D standing wave has $\epsilon = 1$. In each calculation, the interparticle distance equals the size parameter of the particles. Thus, the particles are in contact.

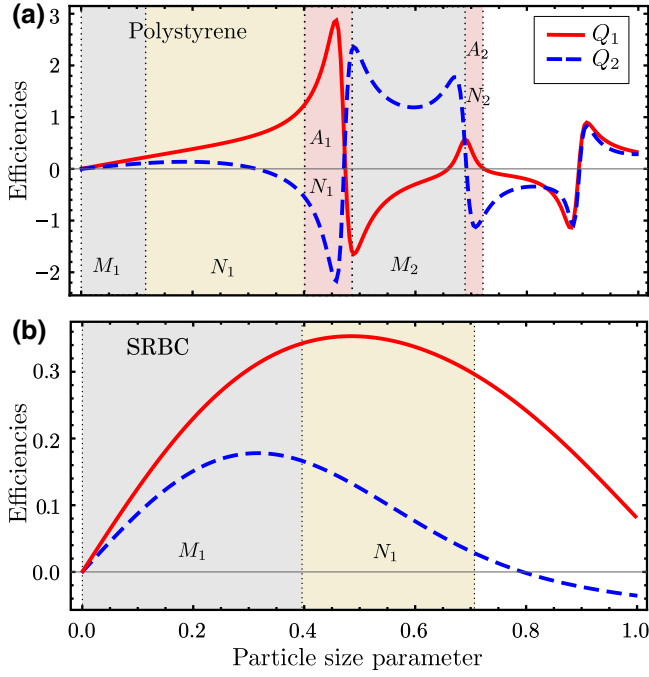


FIG. 2. Radiation-force efficiencies Q_1 and Q_2 versus size parameter of (a) a polystyrene particle and (b) a SRBC in water. The efficiencies are computed with Eq. (13). The labels N_i , A_i , and M_i , with $i = 1, 2$, denote the entrapment bands in pressure nodes, antinodes, and midpoints in nodal lines, respectively.

This configuration results in the largest secondary radiation forces between the particles, given that they decay as an inverse power law of the interparticle distance [33]. It is worth mentioning that the effects of van der Waals and contact forces between the particles are not considered here. The primary radiation forces are computed using Eq. (14), while the secondary forces are numerically evaluated using the interaction beam-shape coefficients (see Appendix B) in the radiation-force efficiencies in Eq. (11).

We show the total (primary + secondary) and secondary radiation-force efficiencies along the x axis of two polystyrene particles [Fig. 3(a)] and two SRBCs [Fig. 3(b)] with size parameters $\xi = 0.4$. The particle positions vary

TABLE II. Formation of trap points for polystyrene particles and SRBCs with respect to the size parameter $\xi = 2a/\lambda$ according to Fig. 2.

Trap	Size parameter range	
	Polystyrene	sRBC
Midpoint	$M_1: 0.00 < \xi \leq 0.10$	$0.00 < \xi < 0.39$
	$M_2: 0.47 \leq \xi < 0.69$	not applicable
Node	$N_1: 0.10 < \xi < 0.47$	$0.39 \leq \xi < 0.71$
	$N_2: 0.69 \leq \xi \leq 0.71$	not applicable
Antinode	$A_1: 0.41 \leq \xi < 0.47$	not applicable
	$A_2: 0.69 \leq \xi \leq 0.71$	not applicable

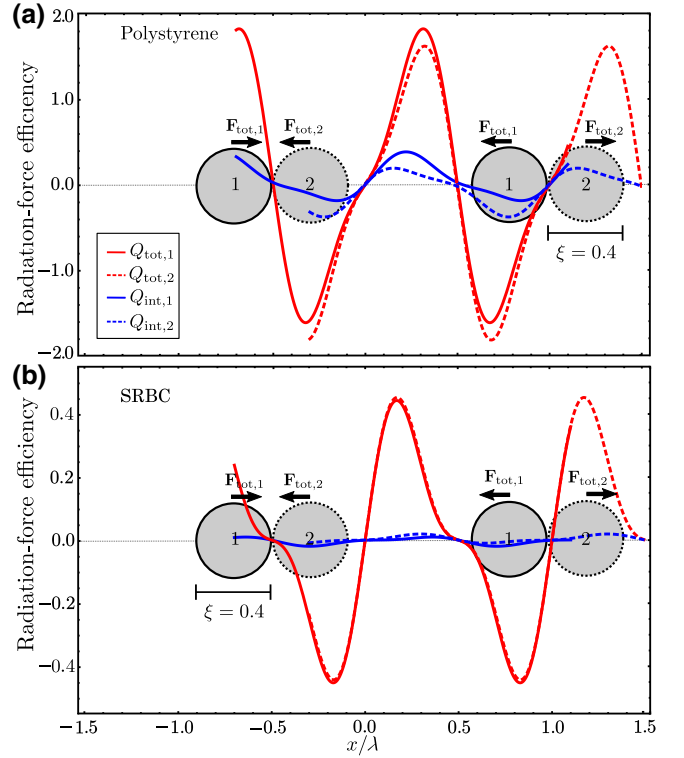


FIG. 3. The total ($Q_{\text{tot}} = Q_{\text{rad}} + Q_{\text{int}}$) and secondary (Q_{int}) radiation-force efficiencies of (a) two polystyrene particles and (b) two sRBCs as a function of their position along the x -axis. The particles' size parameters are $\xi = 0.4$. Circles labeled as “1” and “2” depict the particles and vectors (black arrows) represent the total forces acting on them. The contact points are shown at a node ($x_c = -0.5\lambda$) and antinode ($x_c = \lambda$).

in the intervals $-0.7 \leq x \leq 1.3$ (particle 1) and $-0.3 \leq x \leq 1.5$ (particle 2). Their contact point is illustrated at a node ($x_c = -0.5\lambda$) and antinode ($x_c = \lambda$). While antinodes are the center of unstable regions, nodes are equilibrium points. The contribution of the secondary to the total force is measured through the ratio between their peak-to-peak amplitudes, which values $\rho = 0.15$ (polystyrene) and $\rho = 0.05$ (SRBC).

Other graphical results considering different size parameters are not shown here for brevity. Instead, we present their secondary radiation-force contribution parameter. Firstly, we analyze polystyrene particles for which we have $\rho = 0.17$ ($\xi = 0.41$), $\rho = 0.18$ ($\xi = 0.43$), and $\rho = 0.16$ ($\xi = 0.44$). When $\xi = 0.46$, we have $\rho = 1.25$. However, we are not showing here the primary and secondary radiation forces that are out of phase, yielding a total force of about the same magnitude as the secondary force. Additionally, for size parameters $\xi < 0.4$, the contribution parameter is limited to $\rho < 0.15$ and approaches zero as ξ decreases. We also analyze the secondary radiation force of two particles in contact along the $y = x$ line. The contribution of the secondary radiation force is smaller than that

for particles on the x axis. We conclude that the secondary radiation forces of two particles in contact with $\xi < 0.46$ are smaller than 18% of the total forces on them, regardless of the orientation of their center-to-center line. Secondly, considering SRBCs with size parameter $\xi \leq 0.7$, we find an upper limit for the secondary force contribution as $\varrho \leq 0.08$.

C. One cell per acoustic well patterning

To determine the largest particle that can be, in principle, patterned in the OCPW configuration, we assume that

- (i) All particles are identical;
- (ii) All acoustic potential wells are occupied;
- (iii) The particle diameter $2a$ should be smaller than the distance d between the nearest acoustic potential wells, which means $\xi < d/\lambda$.

According to the conditions in Eq. (18), the potential wells can appear in nodes, antinodes, and midpoints. From Eqs. (2) and (3), we find that the distance between the nearest nodes, antinodes, and midpoints are

$$d = \begin{cases} 0.71\lambda, & \text{node to node or antinode to antinode,} \\ 0.50\lambda, & \text{node to antinode,} \\ 0.50\lambda, & \text{midpoint to midpoint.} \end{cases} \quad (23)$$

These distances do not depend on the particle physical properties. However, the fact that a potential well may take place in a node, antinode, or midpoint is related to the wave frequency and particle size as well as its mechanical properties.

To proceed with the OCPW analysis for polystyrene particles, we have to determine where the acoustic potential wells will be formed by following Table II. Rayleigh particles with size parameter in the range $\xi \leq 0.10$ (M_1 band) tend to cluster together within the potential wells around midpoints. Thus, these particles are not patterned in the OCPW arrangement. Mie particles in the range $0.10 < \xi < 0.41$ (N_1 band) satisfy the OCPW condition (iii) because $\xi < d/\lambda = 0.71$. When $0.41 \leq \xi < 0.47$ (N_1, A_1 band) and $0.47 \leq \xi \leq 0.5$ (M_2 band), the condition (iii) is also fulfilled as $\xi < d/\lambda = 0.5$. For particles with $0.5 < \xi < 0.69$ (M_2 band), the condition (iii) cannot be met as $\xi > d/\lambda = 0.5$. The primary radiation force forms trapping points in the range $0.1 < \xi < 0.47$. However, we note in Sec. III B that, when $\xi > 0.4$, the secondary radiation-force effects become more significant. These effects include attractive and repulsive interaction forces that are likely to disturb the OCPW patterning.

We now analyze the patterning of SRBCs in a waterlike solution. According to Table II and Eq. (23), the condition (iii) is satisfied if SRBCs are patterned in midpoints with

$0 < \xi < 0.39$ (M_1 band) or in nodes with $0.39 < \xi < 0.71$ (N_1 band). If we disregard Rayleigh particle trapping, the range of SRBC patterning is $0.1 < \xi < 0.71$, which is larger than the polystyrene range.

In Fig. 3, we see that the particles can be set apart only if their contact point x_c is initially an antinode. In this case, the radiation forces are in opposite directions as depicted for $x_c = \lambda$. If x_c is in the other position, the particles are likely to remain bound together. This result suggests that the OCPW patterning is highly dependent on the initial spatial configuration of the particles.

IV. EXPERIMENTAL RESULTS

Figure 4 shows the BAW device that is used for experimental patterning of polystyrene particles. The device consists of four piezoelectric transducers (PZT NCE51, $15 \times 2 \times 1 \text{ mm}^3$, Noliac, Denmark) forming an open chamber of dimensions $18 \times 18 \times 2 \text{ mm}^3$ in a polyethylene terephthalate square plate. A glass coverslip is attached to the bottom of the device with a thin layer of adhesive (Fixogum, Marabu GmbH, Germany). The transducers are wired in parallel and driven by a signal generator (Model 33220A, Agilent Technologies, USA) and amplifier (Model 75A250A, Amplifier Research, USA) with a sinusoidal signal of frequency 6.5 MHz and peak-to-peak voltage amplitude between 10 and 16 V_{pp} . Each transducer generates a near planar traveling ultrasonic wave of wavelength $\lambda = 230 \text{ }\mu\text{m}$. As a result, a 2D standing wave is formed within the acoustic chamber ($78\lambda \times 78\lambda$).

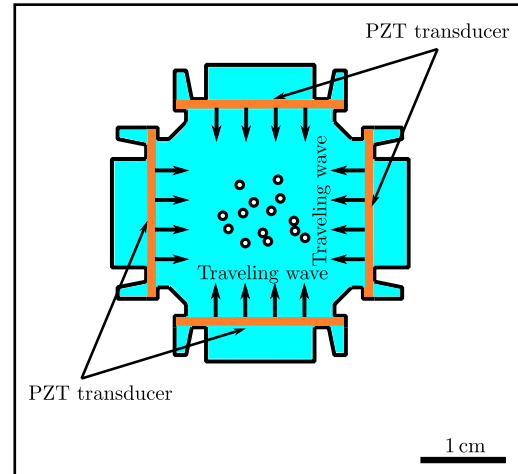


FIG. 4. Schematics of the BAW device for patterning particles. It consists of four piezoelectric transducers (orange rectangles) forming an acoustic chamber of $18 \times 18 \times 2 \text{ mm}^3$, mounted on a polyethylene terephthalate laminate. The transducers are wired in parallel and driven by a sinusoidal signal. Particles (black and white circles) are immersed in distilled water shown in blue. A glass coverslip is attached with adhesive to the bottom of the device.

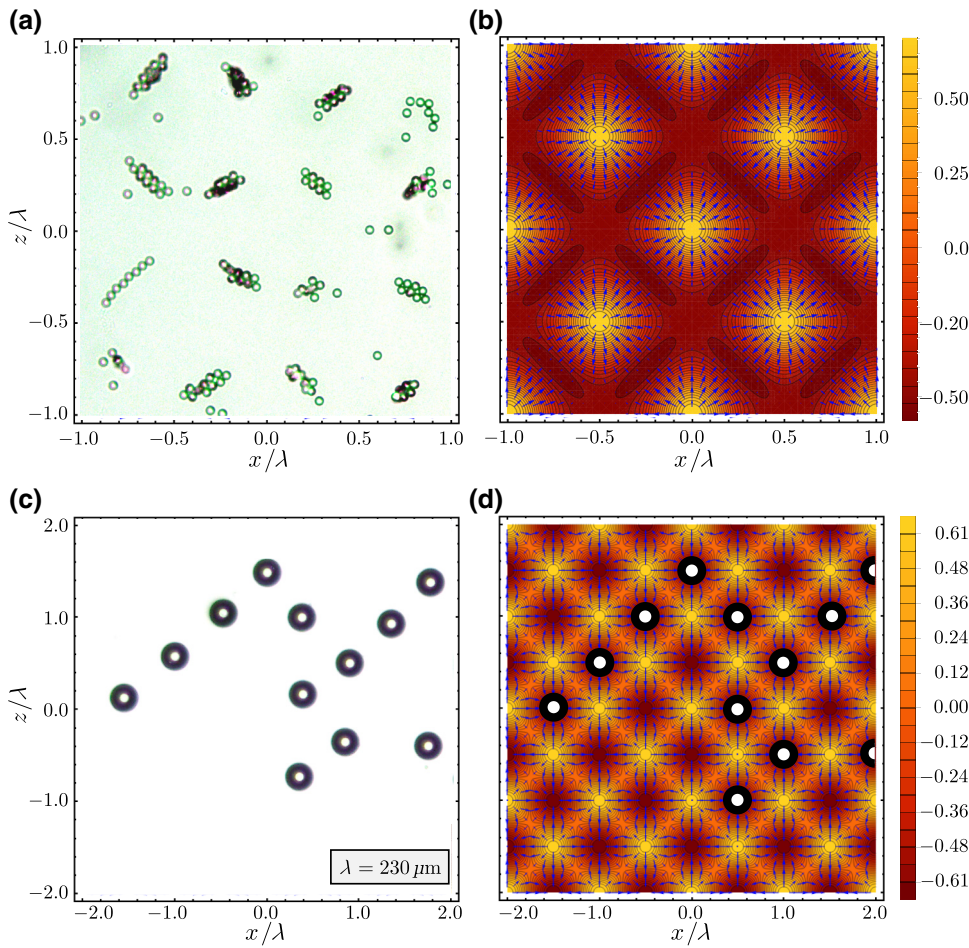


FIG. 5. Micrographs of the central area of the acoustofluidic device containing polystyrene particles with diameter of (a) $10\ \mu\text{m}$ ($\xi = 0.043$) and (c) $75\ \mu\text{m}$ ($\xi = 0.32$) that are immersed in distilled water. (b),(d) The corresponding theoretical predictions for the radiation-force vector field (blue arrows) given by Eqs. (12a) and (12b), and the acoustic energy landscape (background contour plot) computed with Eq. (15) and normalized to $3V_1E_0/8ka$.

An inverted microscope (Olympus CKX53, Japan) is used for making optical imaging of the patterned particles in the device central area ($1 \times 1\ \text{mm}^2$ or $4.3\lambda \times 4.3\lambda$). Two solutions of distilled water with particles of diameter $10\ \mu\text{m}$ (Rayleigh particle, $\xi = 0.043$) and $75\ \mu\text{m}$ (Mie particle, $\xi = 0.32$) are prepared and injected into the acoustic chamber using a pipette (Eppendorf, Germany). After injection, we wait 5 min for the particles to sediment onto the glass substrate. Subsequently, we set the peak-to-peak voltage $V_{\text{pp}} = 10$ and $16\ \text{V}$ for the experiments of, respectively, the Rayleigh and Mie particles.

The micrographs of the Rayleigh and Mie particle patterns are shown in Figs. 5(a) and 5(c), respectively. The corresponding acoustic energy landscapes and radiation-force vector fields (blue arrows) are depicted in Figs. 5(b) and 5(d). The energy landscapes are calculated with Eq. (15), while the radiation force is computed with (12). Following the analysis of Sec. III B, we find that secondary radiation-force amplitudes are smaller than 12% of those of the total force when $\xi \leq 0.32$. Hence, the secondary force effects are neglected here. Note that, despite other forces such as friction (between particles and the glass slide) and Stokes's drag that may act on the particles as

well, the primary radiation force sets them to move toward potential wells. We see that the acoustic patterning of both Rayleigh ($\xi = 0.043$) and Mie ($\xi = 0.32$) particles is in good agreement with theoretical predictions. In all experimental trials with Rayleigh particles (at least 20 repetitions), the particles are always arranged around midpoints in a 2D diamond shape. This result lends support to previous findings regarding the acoustic patterning of Rayleigh particles in water [26] and in hydrogel [11]. While on occasions such as that shown in Fig. 5(c), the OCPW patterning is observed in our experiments with $\xi = 0.32$, on other occasions, multiple particles are clustered in some of the stable locations. Hence, repeatable and consistent OCPW is not achieved. The acoustic energy landscape in Fig. 5(d) shows that the trapping occurs in pressure nodes. Minor inconsistencies in a few particle positions are noted and thought to be due to effects of friction between the particle and the glass coverslide. For instance, the experimental result in Fig. 5(c) illustrates a particle centered at $(0.5\lambda, 1.9\lambda)$, while the theoretical prediction in Fig. 5(d) suggests a particle trapped at $(0.5\lambda, 2\lambda)$. In addition, we perform experiments with polystyrene particles with size parameter $\xi \sim 0.45$. Particle clusters are observed. This

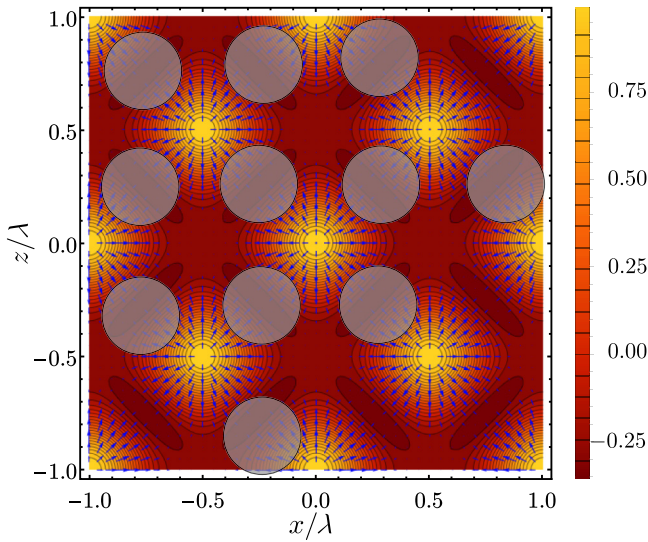


FIG. 6. Acoustic energy landscape (background contour) and radiation-force field (blue arrows) for SRBCs (gray circles) with size parameter $\xi = 0.33$ in a hypotonic solution whose acoustic properties are similar to those of water. The SRBC positions are taken from a central region near the left edge of Fig. 7(b) in Ref. [8].

result corroborates our theoretical predictions in Sec. III B, which state that secondary forces are dominant when $\xi \sim 0.45$.

Our theoretical analysis predicts that polystyrene particles with a size parameter ranging in $0.10 < \xi < 0.4$ move toward pressure nodes under the influence of the primary radiation force. This range covers the one reported by Collins *et al.* [8] for the experimental OCPW patterning of polystyrene particles, $0.25 < \xi < 0.31$. The experimental results are obtained in a SAW rectangular device combining a 2D standing wave and a plane traveling wave. This result suggests that other forces, such as the hydrodynamic flow and radiation force of traveling waves, play a critical role in producing a consistent and repeatable OCPW patterning. In another set of experiments in a SAW device, Brugger *et al.* [13] showed the OCPW arrangement of silica particles in the range of $0.35 < \xi < 0.49$. In this case, a chirped IDT chip is employed to adjust the particle patterning.

We now briefly discuss here the experimental OCPW patterning of SRBCs reported in Ref. [8]. The SRBCs with diameter $2a = 7.5 \mu\text{m}$ and size parameter $\xi = 0.33$ are immersed in a hypotonic solution whose acoustic properties are close to those of water. In Fig. 6, we show the acoustic energy landscape (background contour) and radiation-force field (blue arrows) on SRBCs (gray circles). Their positions are manually measured from a central region near the left edge of Fig. 7(b) in Ref. [8]. The pattern is compatible with our prediction in Table II: SRBCs with $\xi = 0.33$ in a waterlike solution are trapped in midpoints.

V. SUMMARY AND CONCLUSIONS

A theoretical model for the 2D particle patterning produced by two orthogonal standing waves is presented. The standing waves generate acoustic traps by means of the primary radiation force acting on a particle with a size comparable to the wavelength and immersed in a liquid. We demonstrate that the radiation force is a conservative force by obtaining its potential function. The minima of the radiation-force potential correspond to acoustic traps. Our model reveals that particles can be trapped in pressure nodes, antinodes, and midpoints. An exception to this rule are core-shell particles that do not respond to the acoustic radiation force [38]. Trapping position depends on the mechanical parameters of the particle and the surrounding liquid (density and speed of sound). It also depends on the particle size with respect to the wavelength, $\xi = 2a/\lambda$.

With the developed model, we analyze the acoustic patterning of polystyrene particles. We also consider the effects of the secondary radiation force. For polystyrene particles with size parameter $\xi < 0.4$, the amplitude of these forces is up to 15% of the total force. It becomes even smaller as ξ decreases. Thus, we see that in the range $0.10 < \xi < 0.4$, stable traps are formed in pressure nodes. The range for SRBCs, with no significant influence of the secondary radiation force, is larger $0.10 < \xi < 0.71$. In a set of experiments with patterning polystyrene particles immersed in distilled water, we find that Rayleigh particles always form a 2D diamond pattern, whereas Mie particles with $\xi = 0.32$ are patterned at pressure nodes.

In conclusion, our method furnishes insights on the 2D acoustic patterning of particles with a size comparable to the wavelength. The obtained results considerably simplify the analysis of acoustic patterning compared to that based on numerical simulations. They also establish an extension of the patterning theory beyond Gor'kov's potential method, which can be used for Rayleigh particles only. Our findings also provide a useful tool to investigate the conditions for the OCPW configuration. This type of tool is of particular interest for the use of acoustofluidic technology as a platform for massive parallel single-cell analysis and tissue engineering.

ACKNOWLEDGMENTS

This work is partially supported by the Brazilian agency Conselho Nacional de Desenvolvimento Científico e Tecnológico—CNPq (Grants No. 401751/2016-3 and No. 307221/2016-4) and the Royal Society of London, UK (Newton Fund, Grant No. NA160200).

APPENDIX A: BEAM-SHAPE COEFFICIENT

Consider a traveling plane wave $e^{i\mathbf{k}\cdot\mathbf{r}}$ with an arbitrary wavevector $\mathbf{k} = k(\sin\alpha\cos\beta\mathbf{e}_x + \sin\alpha\sin\beta\mathbf{e}_y + \cos\alpha\mathbf{e}_z)$, where α and β are the polar and azimuthal

angles. The partial-wave expansion of a traveling plane wave in spherical coordinates is given by

$$e^{i\mathbf{k}\cdot\mathbf{r}} = 4\pi \sum_{n,m} i^n Y_n^m(\alpha, \beta) j_n(kr) Y_n^m(\theta, \varphi). \quad (\text{A1})$$

Using this expression and Eq. (5), we may expand the plane waves along the x and z axes as

$$\begin{bmatrix} e^{ikx} \\ e^{ikz} \end{bmatrix} = 4\pi \sum_{n,m} i^n \begin{bmatrix} Y_n^m(\frac{\pi}{2}, 0) \\ Y_n^m(0, 0) \end{bmatrix} j_n(kr) Y_n^m(\theta, \varphi). \quad (\text{A2})$$

The cosine functions in Eq. (1) can be decomposed as $\cos k(x+x_1) = (e^{ik(x+x_1)} + e^{-ik(x+x_1)})/2$ and $\cos k(z+z_1) = (e^{ik(z+z_1)} + e^{-ik(z+z_1)})/2$. After placing these expressions into Eq. (1) and using Eq. (A2) with the relation $Y_n^{m*} = (-1)^m Y_n^{-m}$, we find

$$p_{\text{in}} = \frac{P_0}{2} \sum_{n,m} [d_{nm} + (-1)^m d_{n,-m}^*] j_n(kr) Y_n^m(\theta, \varphi), \quad (\text{A3})$$

where

$$\begin{aligned} d_{nm} &= 2\pi \\ &\times \left[e^{i(kz_1+n\pi/2)} Y_n^m(0, 0) + e^{i(kx_1+n\pi/2)} Y_n^m(\frac{\pi}{2}, 0) \right]. \end{aligned} \quad (\text{A4})$$

APPENDIX B: INTERACTION COEFFICIENTS

The effective beam-shape coefficients for each particle at \mathbf{r}_i ($i = 1, 2, \dots, N$) are obtained by solving the system of linear equations [33]

$$c_{nm}^{(i)} - \sum_{j=1}^N \sum_{\nu,\mu} s_{\nu,j} S_{n\nu}^{m\mu} c_{\nu\mu}^{(j)} = a_{nm}^{(i)}, \quad (\text{B1})$$

where the primed sum means $j \neq i$, $s_{n,j}$ is the n th-mode scattering coefficient of a particle at \mathbf{r}_j , and $S_{n\nu}^{m\mu}$ is the translation coefficient given in Ref. [33]. It is useful to express Eq. (B1) in matrix form. In so doing, we have to write the beam-shape and translational coefficients regarding one and two indexes, respectively. Consider that the scattering events described by Eq. (7) are truncated at $n = M$. The effective beam-shape coefficients can be reindexed as follows:

$$\begin{aligned} c_1 &= c_{00}^{(1)}, c_2 = c_{1,-1}^{(1)}, c_3 = c_{1,0}^{(1)}, c_4 = c_{1,1}^{(1)}, \dots, \\ c_{(M+1)^2} &= c_{MM}^{(1)}; c_{(M+1)^2+1} = c_{00}^{(2)}, \dots, \\ c_{2(M+1)^2} &= c_{MM}^{(2)}; \dots, c_{N(M+1)^2} = c_{MM}^{(N)}. \end{aligned} \quad (\text{B2})$$

Likewise, $a_1 = a_{00}^{(1)}$, $a_2 = a_{1,-1}^{(1)}$, \dots , $a_{N(1+M)^2} = a_{MM}^{(N)}$. We define the beam-shape matrices as

$$\mathbf{a} = (a_1 \ a_2 \ \dots \ a_J)^T, \quad \mathbf{c} = (c_1 \ c_2 \ \dots \ c_J)^T, \quad (\text{B3})$$

with $J = N(1+M)^2$. The translation times the scattering coefficients are structured as an off-block diagonal matrix,

$$\mathbf{T} = \begin{pmatrix} \mathbf{0} & \mathbf{S}_2 & \dots & \mathbf{S}_{N-1} & \mathbf{S}_N \\ \mathbf{S}_1 & \mathbf{0} & \dots & \mathbf{S}_{N-1} & \mathbf{S}_N \\ \mathbf{S}_1 & \mathbf{S}_2 & \ddots & \mathbf{S}_{N-1} & \mathbf{S}_N \\ \vdots & \vdots & \vdots & \mathbf{0} & \vdots \\ \mathbf{S}_1 & \mathbf{S}_2 & \dots & \mathbf{S}_{N-1} & \mathbf{0} \end{pmatrix}, \quad (\text{B4})$$

where $\mathbf{0}$ is the $(1+M)^2 \times (1+M)^2$ -null matrix. The translation matrix \mathbf{T} is a $J \times J$ matrix. Writing $S_{nm}^{(i)} = [\mathbf{S}_i]_{nm}$, we have

$$\begin{aligned} S_{11}^{(i)} &= s_0^{(i)} S_{00}^{00}, & S_{12}^{(i)} &= s_1^{(i)} S_{01}^{0,-1}, \\ S_{13}^{(i)} &= s_1^{(i)} S_{01}^{00}, & S_{14}^{(i)} &= s_1^{(i)} S_{01}^{01}, \\ & & & \vdots \\ S_{(1+M)^2, (1+M)^2}^{(i)} &= s_{(1+M)^2}^{(i)} S_{(1+M)^2, (1+M)^2}^{(1+M)^2, (1+M)^2}. \end{aligned} \quad (\text{B5})$$

Now, Eq. (B1) can be written in the matrix format

$$(\mathbf{I} - \mathbf{T}) \mathbf{c} = \mathbf{a}, \quad (\text{B6})$$

with \mathbf{I} being the unit matrix. The interaction coefficient matrix is given by

$$\mathbf{b} = \mathbf{c} - \mathbf{a}. \quad (\text{B7})$$

Thus, the interaction coefficients are obtained by numerically solving the system of linear equations in Eq. (B6).

To validate the presented method, we show in Fig. 7 the broadside backscattering cross section of two identical rigid spheres with $ka = 2$ computed with the effective coefficients \mathbf{c} . We find excellent agreement between our method and the computed result in Ref. [39].

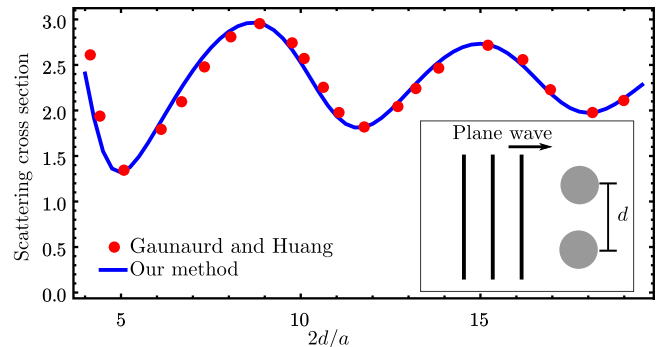


FIG. 7. Broadside backscattering cross section of two rigid spheres of radii a (normalized to πa^2), with $ka = 2$ versus normalized separation distance $2d/a$. Our result is compared to that given by Gaunaud and Huang [39]. Inset: Two-particle scattering problem.

APPENDIX C: MATRIX ELEMENTS OF THE SCATTERING COEFFICIENT

The matrix elements necessary to compute the scattering coefficient in Eq. (8) are given by [28]

$$\begin{aligned}
 e_1 &= i(ka/\omega)j_n'(ka), \\
 e_2 &= -i(\rho_0/\rho_1\omega)k_S^2a^2j_n(ka), \\
 d_{11} &= -i(ka/\omega)h_n^{(1)'}(ka), \\
 d_{12} &= k_Laj_n'(k_La), \\
 d_{13} &= n(n+1)j_n(k_Sa), \\
 d_{21} &= i(\rho_0/\rho_1\omega)k_S^2a^2h_n^{(1)}(ka), \\
 d_{22} &= -4k_Laj_n'(k_La) + [(2n(n+1) - k_S^2a^2)]j_n(k_La), \\
 d_{23} &= 2n(n+1)[k_Saj_n'(k_Sa) - j_n(k_Sa)], \\
 d_{31} &= 0, \\
 d_{32} &= 2[j_n(k_La) - k_Laj_n'(k_La)], \\
 d_{33} &= 2k_Saj_n'(k_Sa) + [(k_Sa)^2 - 2n(n+1) + 2]j_n(k_Sa),
 \end{aligned}$$

where $k_L = \omega/c_L$ and $k_S = \omega/c_S$ are the longitudinal and shear wave numbers inside the particle.

-
- [1] A. Lenshof and T. Laurell, Continuous separation of cells and particles in microfluidic systems, *Chem. Soc. Rev.* **39**, 1203 (2010).
- [2] J. Friend and L. Y. Yeo, Microscale acoustofluidics: Microfluidics driven via acoustics and ultrasonics, *Rev. Mod. Phys.* **83**, 647 (2011).
- [3] J. Shi, D. Ahmed, X. Mao, S. C. S. Lin, A. Lawit, and T. J. Huang, Acoustic tweezers: Patterning cells and microparticles using standing surface acoustic waves (SSAW), *Lab Chip* **9**, 2890 (2009).
- [4] B. Vanherberghen, O. Manneberg, A. Christakou, T. Frisk, M. Ohlin, H. M. Hertz, B. Onfelt, and M. Wiklund, Ultrasound-controlled cell aggregation in a multi-well chip, *Lab Chip* **10**, 2727 (2010).
- [5] X. Ding, P. Li, S.-C. S. Lin, Z. S. Stratton, N. Nama, F. Guo, D. Slotcavage, X. Mao, J. Shi, F. Costanzo, and T. J. Huang, Surface acoustic wave microfluidics, *Lab Chip* **13**, 3626 (2013).
- [6] M. Caleap and B. W. Drinkwater, Acoustically trapped colloidal crystals that are reconfigurable in real time, *Proc. Natl. Acad. Sci. U.S.A* **111**, 6226 (2014).
- [7] C. R. P. Courtney, C.-K. Ong, B. W. Drinkwater, A. L. Bernassau, P. D. Wilcox, and D. R. S. Cumming, Manipulation of particles in two dimensions using phase controllable ultrasonic standing waves, *Proc. R. Soc. A* **468**, 337 (2011).
- [8] D. J. Collins, B. Morahan, J. Garcia-Bustos, C. Doerig, M. Plebanski, and A. Neild, Two-dimensional single-cell patterning with one cell per well driven by surface acoustic waves, *Nat. Commun.* **6**, 8686 (2015).
- [9] B. W. Drinkwater, Dynamic-field devices for the ultrasonic manipulation of microparticles, *Lab Chip* **16**, 2360 (2016).
- [10] L. Tian, N. Martin, P. G. Bassindale, A. J. Patil, M. Li, A. Barnes, B. W. Drinkwater, and S. Mann, Spontaneous assembly of chemically encoded two-dimensional coacervate droplet arrays by acoustic wave patterning, *Nat. Commun.* **7**, 13068 (2016).
- [11] S. M. Naseer, A. Manbachi, M. Samandari, P. Walch, Y. Gao, Y. S. Zhang, F. Davoudi, W. Wang, K. Abrinia, J. M. Cooper, A. Khademhosseini, and S. R. Shin, Surface acoustic waves induced micropatterning of cells in gelatin methacryloyl (GelMA) hydrogels, *Biofabrication* **9**, 015020 (2017).
- [12] M. Prisbrey, J. Greenhall, F. G. Vasquez, and B. Raeymaekers, Ultrasound directed self-assembly of three-dimensional user-specified patterns of particles in a fluid medium, *J. Appl. Phys.* **121**, 014302 (2017).
- [13] M. S. Brugger, S. Grundeen, A. Doyle, L. Theogarajan, A. Wixforth, and C. Westerhausen, Orchestrating cells on a chip: Employing surface acoustic waves towards the formation of neural networks, *Phys. Rev. E* **98**, 012411 (2018).
- [14] S. Lindström and H. Andersson-Svahn, Overview of single-cell analyses: microdevices and applications, *Lab Chip* **10**, 3363 (2010).
- [15] M. Barmatz and P. Collas, Acoustic radiation potential on a sphere in plane, cylindrical, and spherical standing wave fields, *J. Acoust. Soc. Am.* **77**, 928 (1985).
- [16] L. P. Gor'kov, On the forces acting on a small particle in an acoustic field in an ideal fluid, *Sov. Phys. - Dokl.* **6**, 773 (1962).
- [17] G. T. Silva, Acoustic radiation force and torque on an absorbing compressible particle in an inviscid fluid, *J. Acoust. Soc. Am.* **136**, 2405 (2014).
- [18] T. Baasch, I. Leibacher, and J. Dual, Multibody dynamics in acoustophoresis, *J. Acoust. Soc. Am.* **117**, 1664 (2017).
- [19] J. P. K. Armstrong, S. A. Maynard, I. J. Pence, A. C. Franklin, B. W. Drinkwater, and M. M. Stevens, Spatiotemporal quantification of acoustic cell patterning using Voronoi tessellation, *Lab Chip* **19**, 562 (2019).
- [20] T. Hasegawa, Acoustic radiation force on a sphere in a quasi-stationary wave field—theory, *J. Acoust. Soc. Am.* **65**, 32 (1979).
- [21] P. Glynne-Jones, P. P. Mishra, R. J. Boltryk, and M. Hill, Efficient finite element modeling of radiation forces on elastic particles of arbitrary size and geometry, *J. Acoust. Soc. Am.* **133**, 1885 (2013).
- [22] R. Habibi, C. Devendran, and A. Neild, Trapping and patterning of large particles and cells in a 1D ultrasonic standing wave, *Lab Chip* **17**, 3279 (2017).
- [23] T. Baasch and J. Dual, Acoustofluidic particle dynamics: Beyond the Rayleigh limit, *J. Acoust. Soc. Am.* **143**, 509 (2018).
- [24] J. T. Karlsen and H. Bruus, Forces acting on a small particle in an acoustical field in a thermoviscous fluid, *Phys. Rev. E* **92**, 043010 (2015).
- [25] P. B. Muller, R. Barnkob, M. J. H. Jensen, and H. Bruus, A numerical study of microparticle acoustophoresis driven by acoustic radiation forces and streaming-induced drag forces, *Lab Chip* **12**, 4617 (2012).

- [26] S. Oberti, A. Neild, and J. Dual, Manipulation of micrometer sized particles within a micromachined fluidic device to form two-dimensional patterns using ultrasound, *J. Acoust. Soc. Am.* **121**, 778 (2007).
- [27] M. Abramowitz and I. Stegun, *Handbook of Mathematical Functions with Formulas, Graphs, and Mathematical Tables* (Dover Publications Inc., Mineola, NY, 1964).
- [28] J. P. Leão-Neto and G. T. Silva, Acoustic radiation force and torque exerted on a small viscoelastic particle in an ideal fluid, *Ultrasonics* **71**, 1 (2016).
- [29] G. T. Silva, An expression for the radiation force exerted by an acoustic beam with arbitrary wavefront, *J. Acoust. Soc. Am.* **130**, 3541 (2011).
- [30] G. T. Silva, J. H. Lopes, and F. G. Mitri, Off-axial acoustic radiation force of repulsor and tractor bessel beams on a sphere, *IEEE Trans. Ultrason. Ferroelectr. Freq. Control* **60**, 1207 (2013).
- [31] G. T. Silva, A. L. Baggio, J. H. Lopes, and F. G. Mitri, Computing the acoustic radiation force exerted on a sphere using the translational addition theorem, *IEEE Trans. Ultrason. Ferroelectr. Freq. Control* **62**, 576 (2015).
- [32] G. T. Silva and H. Bruus, Acoustic interaction forces between small particles in an ideal fluid, *Phys. Rev. E* **90**, 063007 (2014).
- [33] J. H. Lopes, M. Azarpeyvand, and G. T. Silva, Acoustic interaction forces and torques acting on suspended spheres in an ideal fluid, *IEEE Trans. Ultrason. Ferroelectr. Freq. Control* **63**, 186 (2016).
- [34] P. Mishra, M. Hill, and P. Glynne-Jones, Deformation of red blood cells using acoustic radiation forces, *Biomicrofluidics* **8**, 034109 (2014).
- [35] J. Jarzynski, E. Balizer, J. J. Fedderly, and G. Lee, in *Encyclopedia of Polymer Science and Technology* (John Wiley & Sons, Inc., 2002).
- [36] W. J. Wiscombe, Improved Mie scattering algorithms, *Appl. Opt.* **19**, 1505 (1980).
- [37] G. C. Gaunaurd and H. Überall, RST analysis of monostatic and bistatic acoustic echoes from an elastic sphere, *J. Acoust. Soc. Am.* **73**, 1 (1982).
- [38] J. P. Leão-Neto, J. H. Lopes, and G. T. Silva, Core-shell Particles That are Unresponsive to Acoustic Radiation Force, *Phys. Rev. Appl.* **6**, 024025 (2016).
- [39] G. C. Gaunaurd and H. Huang, Acoustic scattering by a pair of sphere, *J. Acoust. Soc. Am.* **98**, 495 (1995).